Journal of
Marine Science and Engineering

MDPI

Article

A Study of the Relationship between Sand Movement and Flow Field Distribution and Wear Causes in a Multiphase Pump

Xin Guo [1], Guangtai Shi [1,*], Yexiang Xiao [2] and Xunyun Ye [1]

[1] Key Laboratory of Fluid and Power Machinery (Xihua University), Ministry of Education, Chengdu 610039, China; 15884985712@163.com (X.G.)
[2] Department of Energy and Power Engineering, Tsinghua University, Beijing 100084, China
* Correspondence: sgtaixh@126.com

Abstract: The Rosin–Rammler function is used in this paper to model the diameter distribution of sand particles. It investigates the characteristics of sand distribution and identifies the primary factors contributing to wear on flow components in a blade-type multiphase pump, considering varying particle sizes. The result of research shows that the blade head of the impeller and the middle section of the flow passage in the diffuser domain represent primary areas prone to sand particle accumulation. The concentration of sand particles within the diffuser surpasses that within the impeller, yet wear severity and extent are more pronounced in the impeller domain compared to the diffuser domain. Meanwhile, the movement trajectory of sand particles is linked to both shear flow and vortex flow. The wear of the front section of the impeller blade is more severe than the second half. On the pressure surface of the blade, particle Reynolds number emerges as a primary factor influencing wear, while on the suction surface, sand particle concentration plays a dominant role in determining wear. The particle concentration in the diffuser domain is the primary factor influencing wear on both the suction and pressure surfaces. The wear rate in the impeller is primarily influenced by the sand particle Reynolds number, whereas the wear rate in the diffuser domain is affected by a combination of sand particle diameter, sand particle concentration, and sand particle Reynolds number. The research findings possess significant engineering value in terms of enhancing the operational lifespan of multiphase pumps.

Keywords: multiphase pump; sand movement; flow field distribution; wear causes

check for updates

Citation: Guo, X.; Shi, G.; Xiao, Y.; Ye, X. A Study of the Relationship between Sand Movement and Flow Field Distribution and Wear Causes in a Multiphase Pump. *J. Mar. Sci. Eng.* **2024**, *12*, 1203. https://doi.org/10.3390/jmse12071203

Academic Editor: Abdellatif Ouahsine

Received: 7 June 2024
Revised: 11 July 2024
Accepted: 15 July 2024
Published: 17 July 2024

1. Introduction

Multiphase pumps are utilized in the oil extraction industry for centralized conveying, providing a cost-effective and efficient method of transportation. The crude oil obtained from underground reservoirs contains a certain mass proportion of sand particles, which can result in significant abrasion on the components involved in fluid machinery operation.

Scholars have conducted numerous experimental studies on the wear in fluid machinery and have determined that the primary source of wear in fluid machinery is attributed to the motion of solid phases. The primary approach to investigating the motion of solid phases is through conducting flow visualization experiments [1,2]. The velocity of solid particles was captured through ultrasonic velocimetry [3], particle image velocimetry (PIV) [4], phase doppler particle analyzer (PDPA) [5], and high-speed photography [6]. Simultaneously, the experimental investigation also emphasizes the trajectory [7,8] of particle movement and their distribution within the flow passage [9,10]. The factors contributing to wear on parts in the development of wear tests typically encompass particle size, particle shape, and particle concentration [11–13]. The surface wear of the part can be quantified using a non-contact laser contour instrument [14], which enables precise measurement of both the shape and extent of material loss. Additionally, the paint film method [15] can be employed to visually indicate the location of wear. The dynamic evolution of wear sites was investigated by Fujisawa et al. [16] through an experimental study on the erosion process induced by the continuous impact of a jet flow using a water jet device. Additionally, Wang et al. [17] conducted model tests on Invar 36 alloy and Si_3N_4 ceramic balls, thereby supplementing the tribological data of these materials under varying temperatures and loads. This study provides fundamental data for more-precise wear experiments. The feasibility of incorporating diamond-like carbon (DLC) coatings in pumps was assessed by Bueno et al. [18] through the execution of wear and erosion tests. Luo et al. [19] investigated the impact of surface coating thickness on the performance of a solid–liquid two-phase flow centrifugal pump and observed that an increase in coating thickness resulted in a reduction in pump lift and efficiency, while concurrently leading to elevated pressure fluctuations and radial forces within the pump. Through well-designed model tests, accurate and effective data can be obtained; however, this approach necessitates a substantial investment of both time and resources. With the advancement of computational fluid dynamics theory and simulation technology, numerical simulation methods have become prevalent in the field of solid–liquid flow and wear analysis.

The Euler–Euler method and Euler–Lagrange method are commonly employed in simulation calculations to investigate the dynamics of solid–liquid two-phase flows. In the context of the Euler–Euler method, the simulation of solid phase flow can be achieved by employing either the non-uniform model [20] in CFX or the multiphase flow model [21] in Fluent. In the context of the Euler–Lagrange method, three methodologies can be employed, namely, the discrete phase model (DPM) [22], the dense discrete phase model (DDPM) [23], and the discrete element method (DEM) [24]. The Fluent 16.0 software, however, offers a limited range of conventional DEM calculation functions, thereby limiting its ability to perform comprehensive particle collision calculations. To overcome this limitation, the EDEM software can be integrated to enhance the accuracy and completeness of such calculations [25]. First, in the investigation of the solid–liquid two-phase flow's flow field, it has been observed that the presence of the solid phase exerts a discernible influence on both the lift and efficiency of fluid machinery [26,27], thereby further impacting energy conversion within the flow passage [28]. Simultaneously, within the context of solid–liquid two-phase flow, the impact of solid particles against surfaces results in the dissipation of energy and induces varying degrees of abrasion. In this context, Tang et al. [29] investigated the influence of particle size and shape on the impact force exerted on the component surface in a single-channel pump during solid–liquid flow. Gu et al. [30] also investigated the impact of solid particle concentration on centrifugal pump characteristics and the drag reduction characteristics of impellers on non-smooth surfaces. They observed that incorporating pits in the layout of non-smooth surfaces resulted in enhanced drag reduction effects, thereby effectively improving pump performance during the conveyance of solid–liquid mixtures. Additionally, the non-smooth blade model was developed based on the principles of bionics. The performance of the blade model closely resembled that of the prototype blade, while exhibiting an enhanced wear resistance on its surface [31]. The cavitation phenomenon under the gas–solid–liquid three-phase flow has been investigated by other scholars [32], while Zhang et al. [33] conducted an analysis on the impact of gas phase distribution on internal wear in centrifugal pumps. Based on a study investigating the impact of coating thickness on solid–liquid two-phase flow [19], Tao et al. [34] examined the influence of blade thickness on solid–liquid two-phase flow and impeller wear in a ceramic centrifugal pulp pump. They discovered that increasing the blade thickness reduced wear at the leading edge and pressure side of the impeller blade but exacerbated wear at the suction side. In order to validate the accuracy of simulation calculations, simplified model tests are commonly employed in conjunction with simulation results in the literature. For instance, Peng et al. [35] verified the wear location predicted by simulation calculations through wear experiments while investigating solid phase distribution and velocity in centrifugal pumps under varying particle concentrations.

The literature reviewed reveals a significant number of studies on solid two-phase flow in conventional pumps; however, no reports have been found regarding the investigation of blade multiphase mixed-flow pumps. Based on the aforementioned literature review, this study investigates the solid–liquid two-phase flow in a blade-type multiphase pump using the discrete phase model, with the objective of analyzing the distribution characteristics of sand particles within the pump's flow passage, exploring the impact of vortices on sand distribution, and qualitatively and quantitatively analyzing key factors influencing wear in multiphase pumps.

2. Physical Model and Calculation Method

2.1. Model and Meshing

2.1.1. Physical Model

The model in Figure 1 is a blade multiphase pump independently designed by Xihua University, and its main components include a suction chamber, an impeller, a diffuser, and a squeeze chamber. As the pump is an axial multistage type, each stage has the same structure and similar flow, and the main parameters of the pump are shown in Table 1. Taking the first stage of the multistage pump for calculation, the fluid domain is shown in Figure 2. In order to ensure the full development of the flow at the inlet and outlet of the booster unit, the length of the inlet section is three times that of the compress unit, and the length of the outlet section is six times that of the compress unit. The entire fluid domain model is divided into four parts: inlet section, impeller, diffuser, and outlet section.

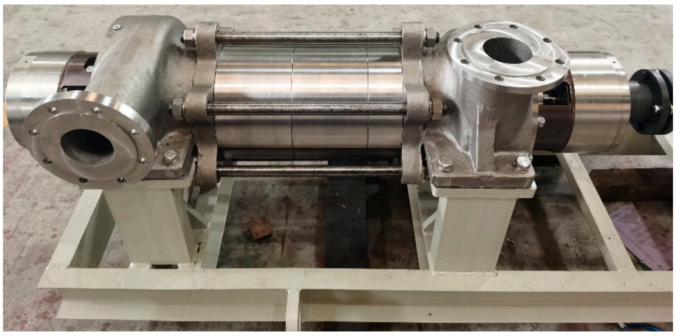

Figure 1. Physical model of multiphase pump.

Table 1. Parameters of multiphase pump.

Parameters	Symbol	Value	Unit
Volume flow rate	Q	200	m^3/h
Rotate speed	n	2980	r/min
Lift	H	30	m
Impeller diameter	D_I	234	mm
Diffuser diameter	D_D	234	mm
Number of impellers	B_I	3	—
Number of diffusers	B_D	11	—

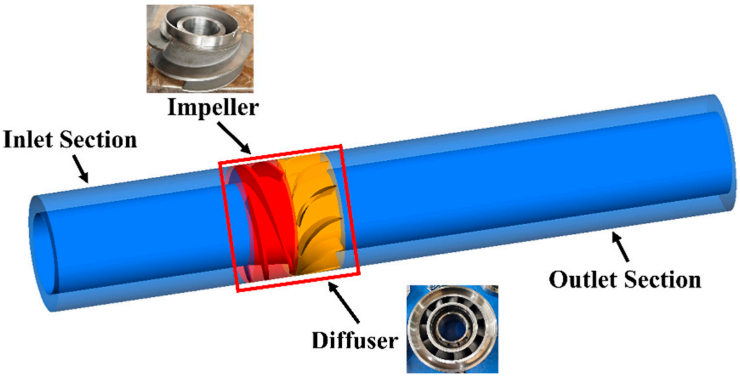

Figure 2. Fluid domain model of multiphase pump.

2.1.2. Meshing

When the finite element method is applied, the partial differential equation is transformed into an equivalent integral form. In this study, the inlet section and outlet section are divided into structural grids using ICEM 16.0 software, while the impeller and diffuser are divided into structural grids using TurboGrid software. The mesh types are all hexahedral-structured meshes. In order to ensure the quality of the near-wall domain's boundary layer mesh, an encryption technique is employed while adopting an O-type topology around the blades. The corresponding mesh configuration is illustrated in Figure 3. The fluid domain models were created in six different sets, each with varying grid numbers. Following the verification of grid independence, Figure 4 presents the pump head and the corresponding grid number for the simulation domain. The numerical simulation results demonstrate that the head of the multiphase pump is minimally influenced by the number of grids. Considering both calculation accuracy and efficiency, this study employs the fourth set of grids for simulation calculations.

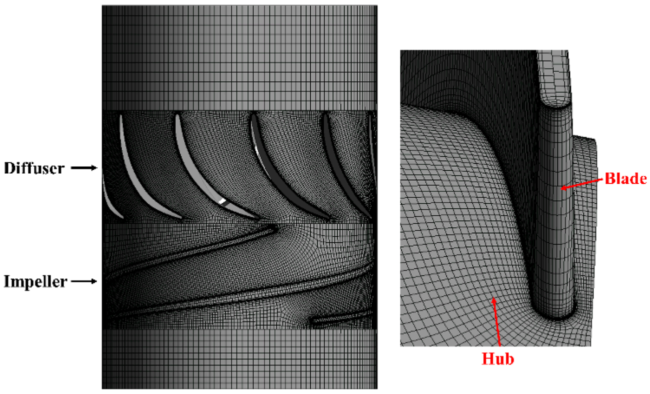

Figure 3. Computational domain grid.

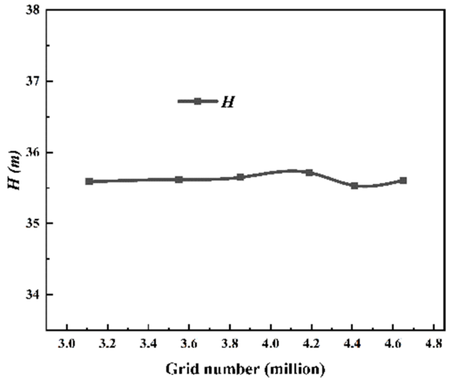

Figure 4. Pump head for different grid numbers.

2.2. Numerical Simulation Method

2.2.1. Continuous Phase Control Equation

In this paper, Fluent software is used to simulate the calculation. The continuous phase flow medium studied in this paper includes crude oil and water. The mixture model regards multiphase flow as a mixture of various phases after mixing. The actual crude oil is also an oil–water emulsion, and the interaction between phases is not clear. Using the mixture model to simulate the oil–water flow conforms to the flow law. When solving the oil–water mixture in the mixing model, the velocity slip and volume force are considered, and the heterogeneous model is used to solve the problem.

The expression of the oil–water two-phase continuity equation is as follows:

$$\frac{\partial \rho_m}{\partial t} + \nabla \cdot (\rho_m u_m) = 0. \tag{1}$$

In the formula, ρ_m is the mixing density and u_m is the average mass velocity.

$$\rho_m = \alpha_{oil}\rho_{oil} + \alpha_{water}\rho_{water} \tag{2}$$

$$u_m = \frac{\alpha_{oil}\rho_{oil}u_{oil} + \alpha_{water}\rho_{water}u_{water}}{\rho_m} \tag{3}$$

In the formula, α_{oil} and α_{water} are the volume fractions of crude oil and water, respectively, ρ_{oil} and ρ_{water} are the density of crude oil and water, respectively, and u_{oil} and u_{water} are the average mass velocity of crude oil and water, respectively.

2.2.2. Discrete Phase Governing Equations

The DPM model is classified as a Euler–Lagrange calculation method, commonly employed in solving fluid flow problems involving particles, and it is particularly suitable for working conditions with particle concentrations of 10% or less. The calculation of particle trajectory in the DPM model adheres to Newton's second law. The formula for calculating particle trajectory and its corresponding force is presented as follows:

$$m_p \frac{du_p}{dt} = F_D + F_B + F, \tag{4}$$

$$F = F_{VM} + F_P + F_R + F_M + F_S, \tag{5}$$

where the subscript p denotes the particle parameter, m_p is the mass of the particle, up is the particle velocity, F_D is the drag force, F_B is the buoyancy caused by gravity, F is the forces on the particle other than the drag force and the buoyancy caused by gravity, F_{VM} is the virtual mass force, F_p is the pressure gradient force, F_R is the Coriolis force and centrifugal force in the rotating system, F_M is the Magnus lift force, and F_S is the Saffman lift force.

In the two-phase flow field, the discrete phase will produce slip velocity v_{slip} in the continuous phase. The calculation formula is as follows:

$$v_{slip} = v_f - v_p. \tag{6}$$

In the formula, v_f is the fluid velocity and v_p is the particle velocity.

During the movement of the particles, the trajectory is most affected by the drag force. The calculation formula is as follows:

$$F_D = m_p \frac{v_{slip}}{\tau_r}. \tag{7}$$

In the formula, the subscript f represents the parameters of the fluid, u is the speed, and τ_r is the particle relaxation time.

$$\tau_r = \frac{\rho_p d_p^2}{18\mu_f} \frac{24}{C_D \mathrm{Re}_p} \tag{8}$$

$$\mathrm{Re}_P = \frac{\rho_f d_p \left| v_{slip} \right|}{\mu_f} \tag{9}$$

In the formula, ρ is the density, d_p is the particle diameter, μ_f is fluid dynamic viscosity, Re_p is the particle Reynolds number, and C_D is the drag coefficient.

In this paper, the shape of the particle is regarded as a sphere, and the calculation formula of the drag coefficient proposed by Morsi and Alexander is adopted. The drag coefficient is as follows:

$$C_D = a_1 + \frac{a_2}{\mathrm{Re}_p} + \frac{a_3}{\mathrm{Re}_p^2}. \tag{10}$$

In the formula, a_1, a_2, and a_3 are empirical constants, using Morsi's recommended values.

The buoyancy caused by the gravity of the particles is calculated as follows:

$$F_B = m_p\left(1 - \frac{\rho_f}{\rho_p}\right)g. \tag{11}$$

In the formula, g is the acceleration of gravity.

The virtual mass force comes from the relative acceleration motion between fluid and particles, which can be expressed as follows:

$$F_{VM} = C_{VM} m_f \left(\frac{du_f}{dt} - \frac{du_p}{dt}\right). \tag{12}$$

In the formula, C_{VM} is the virtual mass coefficient, taking 0.5.

Due to the uneven distribution of pressure in the flow field, there is a pressure difference on the surface of the particles, resulting in a pressure gradient force:

$$F_P = m_p \frac{\rho_f}{\rho_p} u_p \nabla u_f. \tag{13}$$

In rotating machinery, there must be Coriolis force and centrifugal force on the particles. The calculation formula is as follows:

$$F_R = m_p\left(-2\omega \times u_p - \omega \times \omega \times r_p\right). \tag{14}$$

In the formula, ω is the relative angular velocity between particles and fluid, and r_p is the set vector from the particle to the coordinate origin.

When a particle moves in a flow field with a velocity gradient, the particle rotates around its center of mass due to the velocity gradient, and a Magnus lift is generated. When the velocity gradient is perpendicular to the movement direction of the particles, the particles will be affected by the Saffman lift. The calculation formulas of the two forces are as follows:

$$F_M = \frac{1}{2} A_p C_M \rho_f \frac{\left|v_{slip}\right|}{|\omega|}\left[v_{slip} \times \omega\right], \tag{15}$$

$$F_S = K_S 4 r_p^2 \rho_f \left|v_f \frac{\partial V_{fi}}{\partial x_i}\right|^{\frac{1}{2}} \left(V_{fi} - V_{pi}\right) \mathrm{sgn}\left(\frac{\partial V_{fi}}{\partial x_i}\right). \tag{16}$$

In the formula, A_p is the projection area of particles, C_M is the rotational lift coefficient, K_S is the empirical coefficient, and sgn is a symbol function.

2.2.3. Wear Model and Rosin–Rammler Method

The wear of the multiphase pump surface is predicted using the Oka wear model. The Oka model expresses the wear rate as follows:

$$E = E_{90}\left(\frac{V}{V_{ref}}\right)^{k_2}\left(\frac{d}{d_{ref}}\right)^{k_3} f(\gamma), \tag{17}$$

where E_{90} is the impact wear rate of particles at 90°, V is the impact velocity of particles, V_{ref} is the reference velocity, d and d_{ref} are the particle diameter and the particle reference diameter, k_2 and k_3 are the model velocity constant and the model diameter constant, and *f*(γ) is the impact angle function.

The calculation formula of impact angle function is as follows:

$$f(\gamma) = (\sin\gamma)^{n_1}(1 + H_V(1 - \sin\gamma))^{n_2}, \tag{18}$$

where γ is the wall impact angle, H_V is the Vickers hardness of wall material, and n_1 and n_2 are model constants.

The coefficients in the Oka model exhibit variations, catering to different wear prediction scenarios. Specifically, for the erosion of steel particles, Table 2 presents the corresponding coefficient values.

Table 2. Constants of wear formula.

C	Sand-Steel	C	Sand-Steel
E_{90}	6.154×10^{-4}	k_2	2.35
H_V	1.8 (GPa)	k_3	0.19
n_1	0.8	V_{ref}	326 (µm)
n_2	1.3	d_{ref}	104 (m/s)

In order to account for the influence of particles with varying diameters in the calculation, we have employed the Rosin–Rammler (RR) method to characterize the diameter distribution of particles at the inlet of the multiphase mixed transport pump. The mathematical expression for describing particle diameter distribution using RR method is as follows:

$$Y_d = e^{-(d/\overline{d})^n}, \tag{19}$$

where Y_d is the mass fraction, d is the particle diameter, $\overline{d}$ is the average particle diameter, n is the diameter distribution index, and e is a constant.

The particle diameter distribution of this paper was determined using the RR method and is presented in Table 3.

Table 3. Particle diameter distribution.

Parameters	Value	Unit	Parameters	Value	Unit
Max diameter	5	mm	Mean diameter	0.4	mm
Min diameter	6.5×10^{-2}	mm	n	2.53	

2.3. Boundary Conditions

The Z-axis negative gravity acceleration is set to 9.81 m/s^2 in this study. The SST k-ω model is chosen as the turbulence model. The flow passage wall is considered as a non-slip boundary condition. The inlet boundary condition is specified as the speed inlet, and the outlet boundary condition is defined as the pressure outlet. The impeller speed is fixed at 2980 r/min, and the frozen rotor model utilizing the intersection of dynamic and static computing domains is employed.

The coupling solution is established between the discrete and continuous phases, taking into account their interaction. A circular boundary at the inlet section is chosen as the particle incident source, ensuring uniform injection of particles into the flow field from each grid unit's normal vertical direction on the incident surface. The Ipc varies from 0.1% to 10% across ten operational conditions. The incident velocity of the particle is adjusted to match the inlet flow velocity. The particle material is chosen as quartz sand, characterized by a density of 2650 kg/m^3. The density ratio of solid particles to continuous phase medium is about 2.685. The inlet and outlet surfaces of the multiphase pump are designated as "Escape", while the wall surfaces of the flowing parts are referred to as

"Reflect". The calculation of solid–liquid two-phase flow commences by utilizing the stable flow field of fluid flow as the initial state.

Considering the interaction between particles and walls, we adopted the particle-wall collision model proposed by Pagalthivarthi. The recovery coefficients for normal and tangential directions after impact were expressed as polynomial functions of impact angles, with specific formulas presented as follows:

$$e_n = 0.993 - 0.0307\gamma + 0.000475\gamma^2 - 0.00000261\gamma^3, \tag{20}$$

$$e_t = 0.998 - 0.029\gamma + 0.000643\gamma^2 - 0.00000356\gamma^3, \tag{21}$$

where e_n represents the normal recovery coefficient and e_t denotes the tangential recovery coefficient.

3. Experimental Study

3.1. Multiphase Pump Test Bench

The external characteristics of the multiphase pump were tested in the pump testing center of Zigong Industrial Pump Factory. The test system employed a pressure transmitter to measure the inlet and outlet pressures, a flowmeter to measure the pump's flow rate, a speedometer to measure its rotational speed, and a three-phase power meter to measure shaft power. The specific instrument accuracy is detailed in Table 4. The test device used was a four-stage multiphase pump. Since the solid phase content has minimal impact compared to the liquid phase, pure water was chosen as the test medium. Figure 5 illustrates the setup of the external characteristics test system.

Table 4. Testing the accuracy of the instrument.

Instrument	Range	precision	Unit
Inlet pressure gage	−0.1~0.25	±0.02%	MPa
Outlet pressure gage	0~4	±0.06%	MPa
Flow meter	0~380	±0.2%	m^3/h
Tachometer	20~33,000	±0.03%	rpm
Torquemeter	0~800	±0.2%	N·m

Figure 5. Test system of multiphase pump.

3.2. Test Result

To ensure the accuracy of the selected research method, experimental testing and verification of the chosen numerical calculation method is conducted prior to formal calculations. The test measurement results for external characteristics are compared with corresponding simulation results, as depicted in Figure 6. As shown in Figure 6, under design conditions, the multiphase pump exhibits a lift of 158 m and an efficiency of 43%, meeting design requirements. Additionally, external characteristic simulation results for the multiphase pump at flow rates equivalent to 0.7 times and 1.1 times rated flow exhibit similarity to the test results with small overall error near the rated flow, thus indicating the high reliability of the numerical research method selected for further subsequent content investigation.

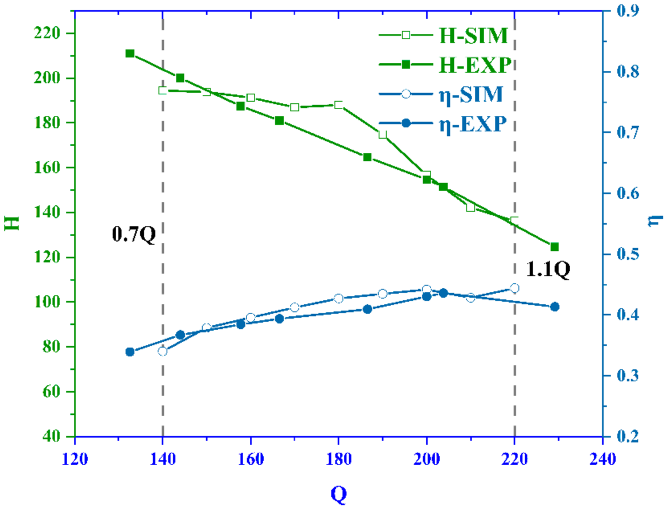

Figure 6. Test results of external characteristics of multiphase pump.

3.3. Wear Model Validation

Due to the high cost associated with conducting the medium erosion test under investigation in this study, several scholars have previously conducted relevant experimental verification on the computational accuracy of the OKA model (Remo et al. [36]). The test system for jet wear tests is shown in Figure 7 below. In the slurry used in the test, it is guaranteed that the particle impact speed is 25 m/s, the particle concentration is 1%, the particle shape is uniform, and the diameter is 1 mm. In the literature, the erosion rate is expressed by the normalized erosion rate:

$$R_{norm} = Q/(V_s \times A), \tag{22}$$

where Q is the volume flow rate (m^3/s), V_s is the particle impact velocity, and A is the apparent erosion area of the sample. The square sample size in the jet test device is 25 mm × 25 mm, the height is fixed, and the impact Angle can be controlled between 15° and 90°. The diameter of the nozzle is 4 mm, and the distance between the nozzle and the sample is 25 mm (see Figure 8).

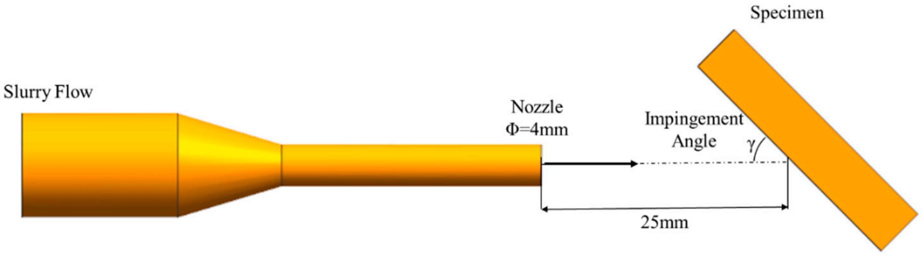

Figure 7. Jet testing apparatus.

Figures 8 and 9 present results obtained from both jet wear testing and Fluent simulation calculations, illustrating erosion patterns as well as normalized erosion rates on specimen surfaces. As shown in Figure 8, the simulated wear shape and area highly coincide with experimental results, indicating that numerical calculation methods can effectively reflect actual particle impacts. Furthermore, in Figure 9, it can be observed that as impact angle increases, the normalized erosion rate initially rises until reaching its maximum value before subsequently decreasing towards stability. A comprehensive analysis comparing quantitative outcomes derived from tests and simulations reveals prediction errors ranging between 0.56% and 23.33%.

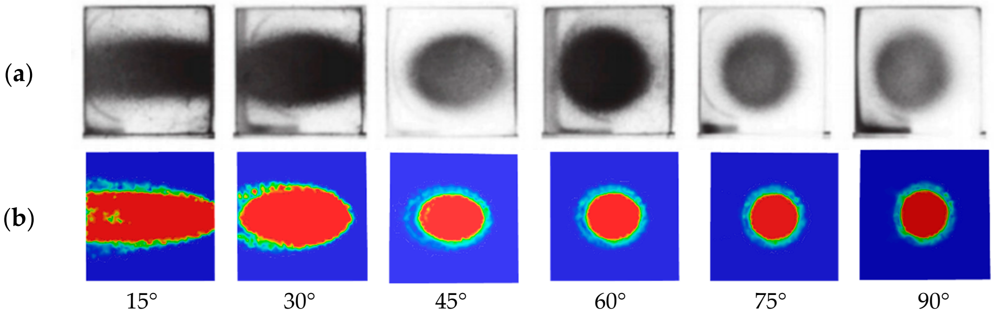

Figure 8. Impact surface morphology of the specimen: (**a**) measured (Remo et al. [36].); (**b**) simulated.

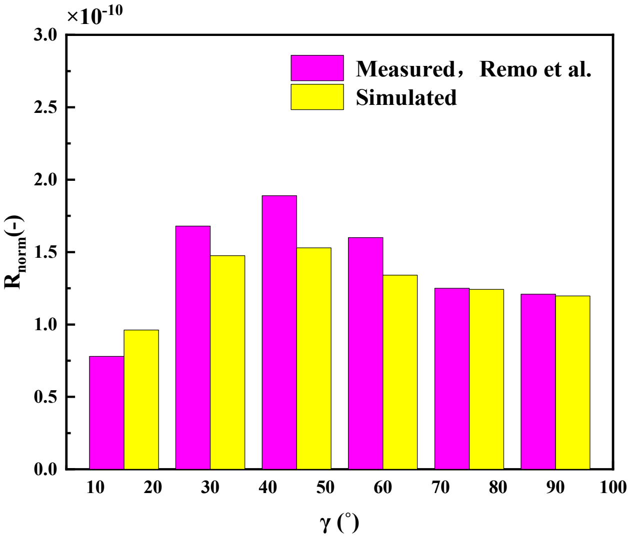

Figure 9. Normalized surface erosion rate of the specimen [36].

4. Sand Particle Distribution inside Multiphase Pump

4.1. The Effect of Sand Concentration on Sand Distribution

The increase in inlet sand particle concentration corresponds to an increase in the number of sand particles entering the pump passage per unit of time, which directly influences the quantity and distribution of sand particles within the passage. To analyze the impact of inlet sand particle concentration on sand particle distribution, we examined the cloud map depicting sand particle mass concentration at 0.5 times the blade height under various conditions (Figure 10). The increase in sand concentration leads to a significant rise in the sand concentration within the flow channel of the multiphase pump. The blade head of the impeller and the central region of the diffuser area are the primary sites for the accumulation of sand particles. The black box in Figure 10 reveals a region of reduced sand concentration situated within the impeller domain. The relationship curve between different sand concentrations and sand mass in the flow passage is depicted in Figure 11. It can be observed that the diffuser contains a higher number of sand particles compared to the impeller across all concentrations.

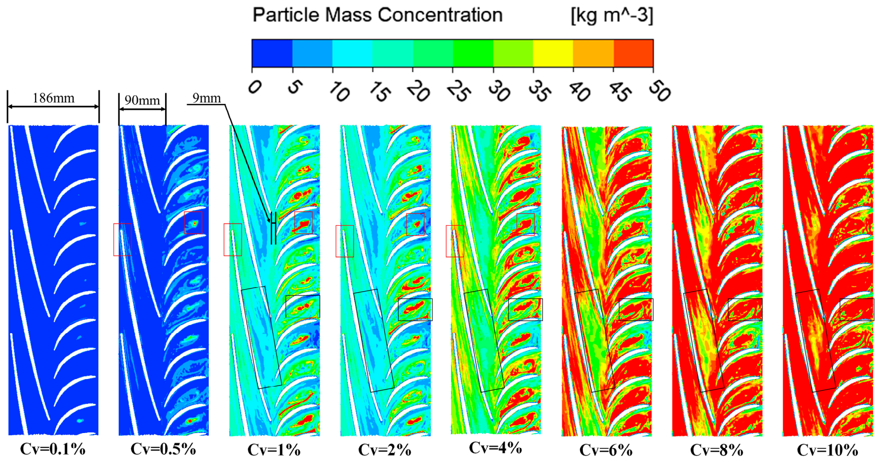

Figure 10. Nephogram of sand particle distribution inside the flow passage.

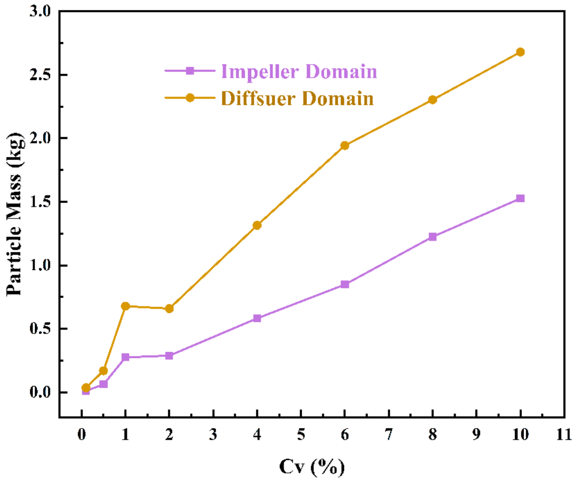

Figure 11. Sand particle mass inside the flow passage.

4.2. The Spatial Distribution of Sand Particles within the Impeller Domain

In order to visually represent the sand particle distribution within the passage, we initially selected the impeller domain's $Y \geq 0$ domain to display a volume nephogram depicting various sand particle mass concentrations. The shaded area in Figure 12a illustrates the chosen scope of the passage. Figure 12b presents an iso-surface nephogram displaying different sand particle mass concentrations. For analysis purposes, we considered inlet sand particle concentrations of 6%, 8%, and 10% as distinct cases, with the sand particle velocity rendered on the surface of each nephogram.

In Figure 12b, when the threshold increases, the sand-particle-occupied space volume increases with the increase in inlet sand particle concentration. As can be seen from the orange oval in Figure 12b, when the threshold is small, a decrease in the concentration of inlet sand particles leads to an expansion of the sand particle distribution area. The increase in inlet sand particle concentration exacerbates the phenomenon of sand particle aggregation in the impeller passage, thereby resulting in a gradual rise in the central mass concentration within the sand particle distribution area. The increase in inlet sand particle concentration within the local area leads to a radial shift in the sand particle distribution towards the rim, as depicted by the red box in Figure 12b. The core of the sand particle aggregation domain is located at the hub, as indicated by the purple box in Figure 12b. Furthermore, with an increase in inlet sand particle concentration, there is a decrease in sand particle velocity within the passage, as observed within the black box in Figure 12b.

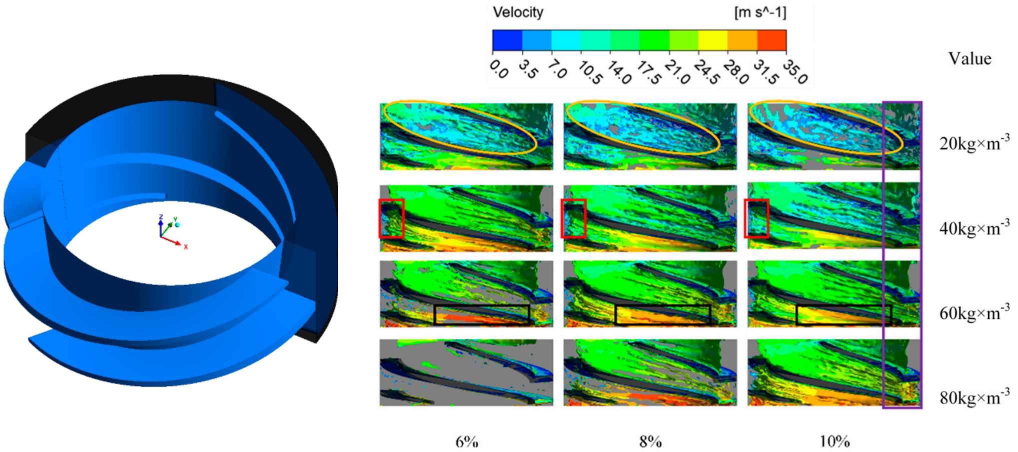

(**a**) (**b**)

Figure 12. Sand particle aggregation phenomenon in the impeller domain: (**a**) flow path diagram; (**b**) iso-surface nephogram of different sand particle mass concentrations.

4.3. The Spatial Distribution of Sand Particles within the Diffuser Domain

The domain within the diffuser domain, characterized by $Y \geq 0$, was selected to illustrate the shear volume nephogram for various sand particle mass concentration values, as depicted in Figure 13. The distribution area of sand particles in the diffuser domain is mainly in the middle of the flow passage. In the black box in Figure 13b, the concentration of the concentrated distribution area of sand particles is between 60 kg $\times$ m^{-3} and 100 kg $\times$ m^{-3}. Figure 13b illustrates that the velocity of iso-face varies with sand particle mass concentrations. Smaller-threshold sand particles exhibit higher velocities and are predominantly located at the diffuser inlet, while larger-threshold sand particles have lower velocities and tend to accumulate in the middle of the passage. Notably, within the diffuser domain, sand particles display a spiral belt-like distribution in the middle of the passage and a flaky distribution near the rim of this domain. The velocities near the rim are significantly higher than those observed within the passage, as indicated by the red box in Figure 13b.

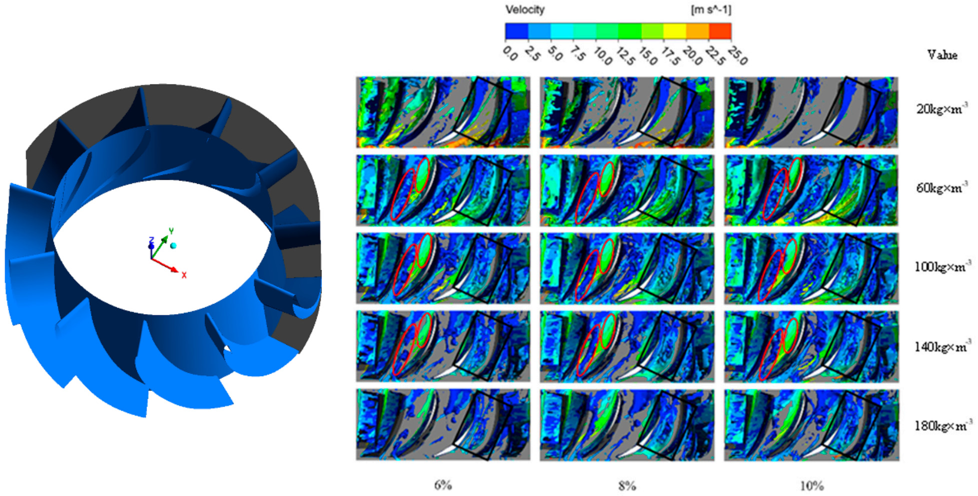

(**a**) (**b**)

Figure 13. Sand particle aggregation phenomenon in the diffuser domain: (**a**) flow path diagram; (**b**) iso-surface nephogram of different sand particle mass concentrations.

5. The Effect of Vortex on Sand Particle Distribution

5.1. The Effect of Vortex on Axial Sand Particle Distribution in a Multiphase Pump

The flow channel vortex plays a crucial role in influencing the flow behavior of multiphase pumps. Due to the intense momentum exchange between sand particles and the liquid phase, the impact of vortices on sand particle distribution within solid–liquid two-phase flows holds significant importance. The mass concentration of sand particles at different blade heights and the vortex distribution in the flow passage of the multiphase pump are depicted in Figure 14, considering an inlet sand particle concentration of 10% (here, Span = 0.1, 0.5, and 0.9, respectively, represent positions near the hub, middle of the flow passage, and near the shroud). According to the Ω method, a lower threshold value on the plane leads to an increased characterization of shear vortex bands, whereas a higher threshold value results in a greater characterization of rigid rotation vortex bands.

$$\Omega = \frac{\|B\|_F^2}{\|A\|_F^2 + \|B\|_F^2}, \tag{23}$$

$$A = \frac{1}{2}\left(\nabla V + \nabla V^T\right), \tag{24}$$

$$B = \frac{1}{2}\left(\nabla V - \nabla V^T\right), \tag{25}$$

where A is the symmetric part of the velocity gradient tensor ∇V, B is the anti-symmetric part, and $\|\cdot\|_F$ is the Frobenius norm.

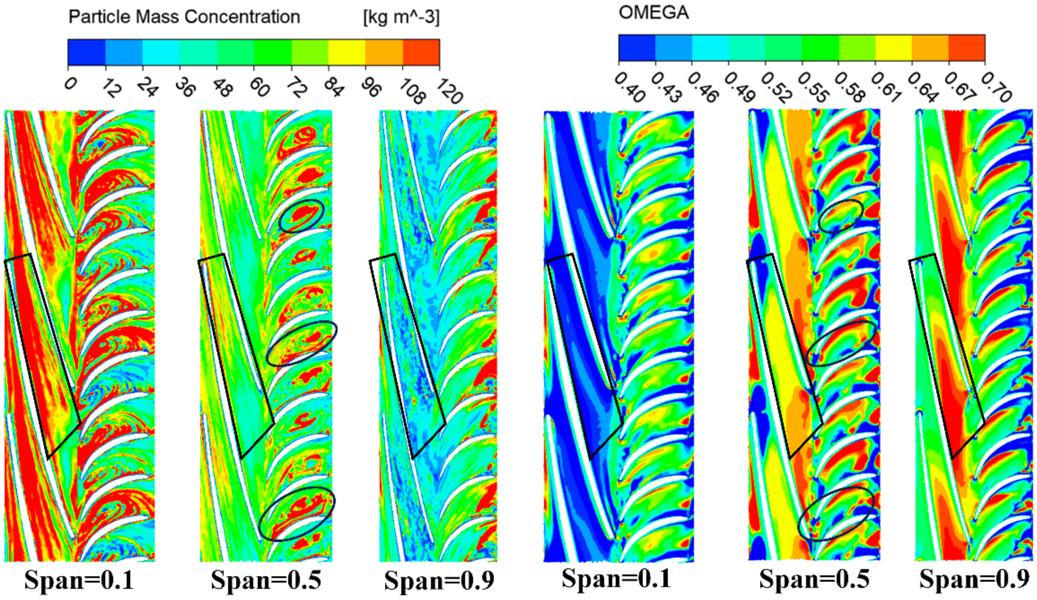

Figure 14. Sand particle mass concentration and vortex distribution in the flow passage.

It can be seen from the sand particle mass concentration distribution cloud chart at different blade heights that the sand particle distribution in the impeller domain is concentrated in the hub, and the sand particle is less close to the shroud. The sand particle distribution in the diffuser domain is partly distributed in the middle of the flow passage and the outlet of the diffuser. Significant differences in vortex distribution between the impeller and diffuser domains are observed at various blade heights in the vortex distribution nephogram. In the impeller domain, the shear vortex is predominantly concentrated near the hub, while the rigid rotating vortex dominates most of the central area within the passage. In the diffuser domain, the shear vortex primarily aligns along the diffuser wall, whereas the rigid rotating vortex mainly occupies the central portion of the passage.

The influence of different vortex structures on sand particle distribution was analyzed by comparing the sand particle distribution area with the vortex distribution area. By comparing the details of the two cloud images, it is evident that the spatial distribution of the shear vortex within the impeller domain exhibits a remarkable congruence with the sand particle distribution, as depicted in the enclosed black box in Figure 14.

5.2. The Effect of Vortex on Circumferential Distribution of Sand in Impeller of Multiphase Pump

In order to investigate the impact of channel vortex on sand particle distribution, with an inlet sand particle concentration of 10%, we initially selected five sections at radial average distances within a single channel in the impeller domain to characterize variations in sand particle behavior along the channel direction and track the evolution of channel vortex movement. The positions and sizes of these five sections within the channel are illustrated in Figure 15.

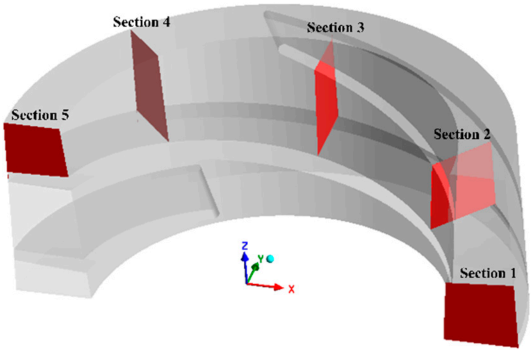

Figure 15. Diagram of the five sections in the impeller.

The sand distribution and vortex distribution on the section were investigated, as illustrated in Figure 16. The sand particles in Section 1 at the impeller inlet still maintain their original distribution characteristics due to the homogeneous dispersion of sand particles in the flow passage ahead of the impeller, as depicted in Figure 16. From the inlet to the outlet of the flow passage, sand particles gradually migrate towards the hub, resulting in the gradual integration of scattered sand micro-clusters. Simultaneously, the distribution area of shear flow progressively contracts towards the hub, leading to the formation of a substantial vortex under its influence. The distribution of sand particles in the five sections exhibits a strong correlation with the shear flow, suggesting a direct relationship between the movement trajectory of sand particles and the shear flow. Due to the main work area of the pump in the impeller, the velocity of the fluid is large, so the shear vortex in the impeller has a greater impact on the sand particles. Conversely, minimal sand particle distribution is observed within the vortex distribution area on the sections, indicating that vortex motion within the impeller domain leads to a more concentrated dispersion of sand particles.

5.3. The Effect of Vortex on Circumferential Distribution of Sand in Diffsuer of Multiphase Pump

The diffuser domain in the multiphase pump is characterized by the selection of five sections, which are distributed evenly along the axial direction and maintain a consistent axial spacing from the inlet to the outlet. These sections are designated as illustrated in Figure 17.

Figure 18 shows the sand particle and vortex distributions in the five sections of the diffuser domain. The distribution of sand particles and vortices from the inlet to the outlet appears to be disordered, as depicted in Figure 18. Specifically, both vortex zones exert a discernible influence on the movement of sand particles. The distribution of sand particles at the inlet maintains the characteristics observed in the impeller domain. However, upon entering the diffuser domain, a significant influence from the vortex within the diffuser (refer to Figure 14) is observed. As a result, sand particles in the middle of the flow channel tend to concentrate towards the center of this vortex, while those at the outlet are predominantly distributed along the wall. The distribution of the vortex in the flow passage is predominantly concentrated in the middle, as depicted in Figure 18. Moreover, a decrease in vortex intensity can be observed at both the inlet and outlet. The influence of the vortex in the diffuser domain on the movement of sand particles is evident as these particles are observed to be entrained by the vortex. The main reason is that the fluid kinetic energy is transformed into pressure energy in the diffuser, which inevitably produces a large number of high-energy vortices, and the vortices with higher energy have a greater impact on the movement and distribution of sand particles.

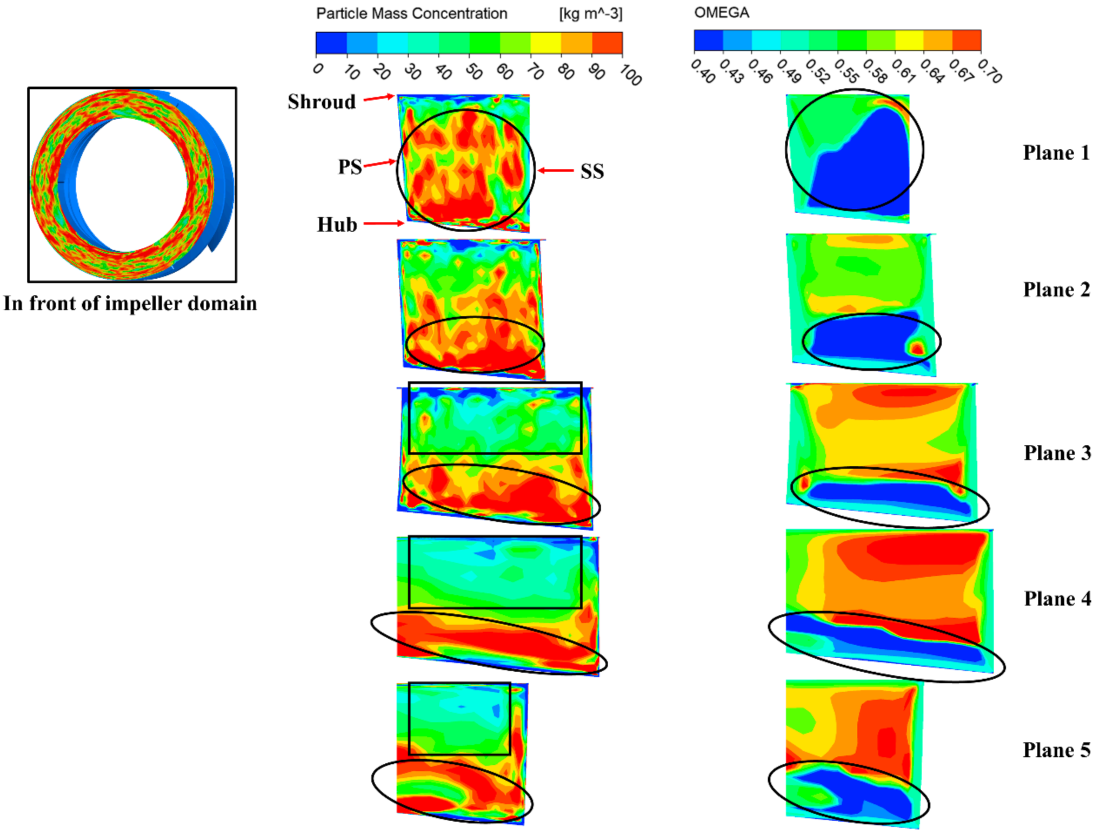

Figure 16. Sand particle distribution and vortex distribution on the five sections in the impeller domain.

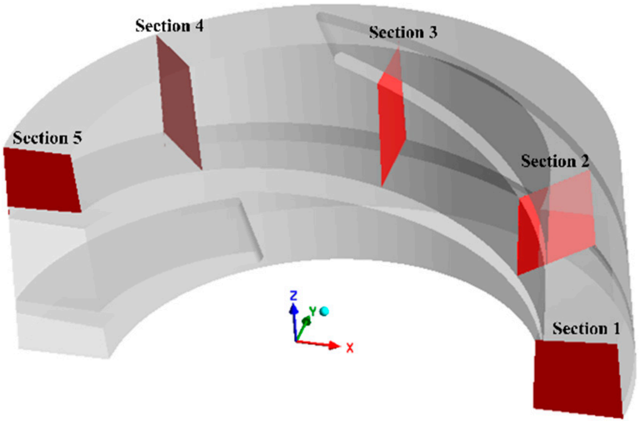

Figure 17. Diagram of the five sections in the diffuser.

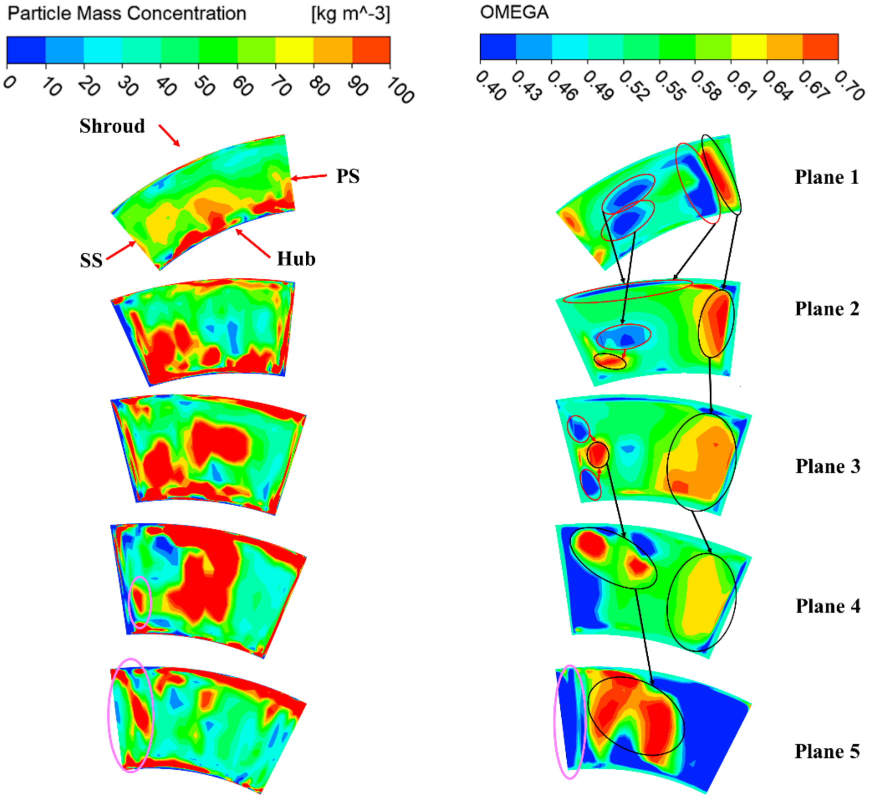

Figure 18. Sand particle distribution and vortex distribution in the five sections of the diffuser domain.

6. Wear Distribution of Multiphase Pump

6.1. Wear Distribution on Blade Surface

The distribution of sand particles in the flow passage is influenced by varying concentrations of sand, which subsequently leads to wear on the blade surface. The wear distribution on the impeller blade surface was analyzed under different concentrations of sand particles, as illustrated in Figure 19. The wear of the pressure surface and suction surface of the impeller blade exhibits significant variations under different operational conditions, as illustrated in Figure 19. When the sand concentration is low, the wear area of the pressure surface is smaller than that of the suction surface, with predominant wear on the pressure surface occurring at the blade's trailing edge, while predominant wear on the suction surface occurs in the middle section of the blade. The increase in sand concentration resulted in evident wear on the outer edge of the leading section of the pressure surface, as indicated by the black box in Figure 19. Conversely, the wear on the suction surface increases with concentration, exhibiting minimal variation in wear area size but a significant increase in wear severity. Additionally, there is a slight wearing of the strip at the trailing edge of the suction surface, as indicated by the red box in Figure 19.

The nephogram of wear distribution on the surface of the diffuser under varying concentrations of sand particles is depicted in Figure 20. The wear on the pressure surface of the diffuser is evidently more pronounced than that on the suction surface, as depicted in Figure 20. The wear on the pressure surface primarily occurs along the diffuser's edge. As the sand concentration increases, the wear area gradually extends towards the blade's center. The wear of the diffuser suction surface primarily occurs on the inlet surface, and the increase in sand particle concentration has a limited effect on the expansion of the worn area. Based on Figures 19 and 20, it can be observed that the impeller domain exhibits more severe wear area and degree compared to the diffuser domain.

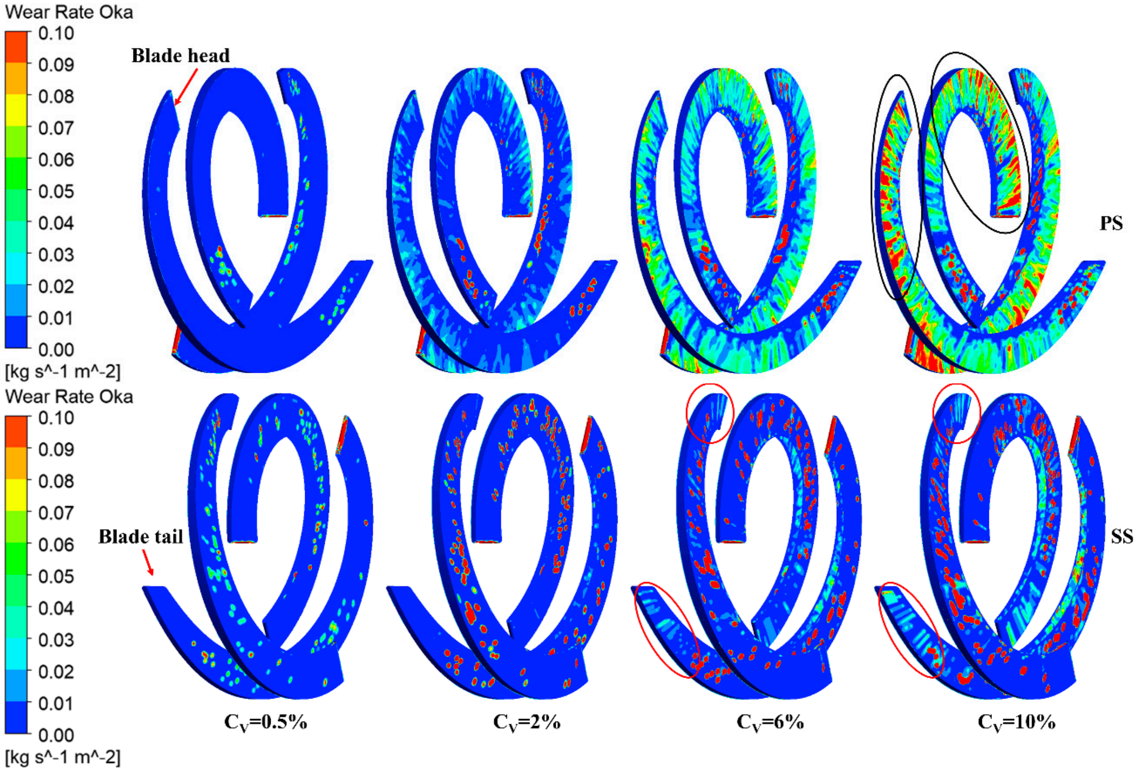

Figure 19. Wear distribution of impeller blade surface.

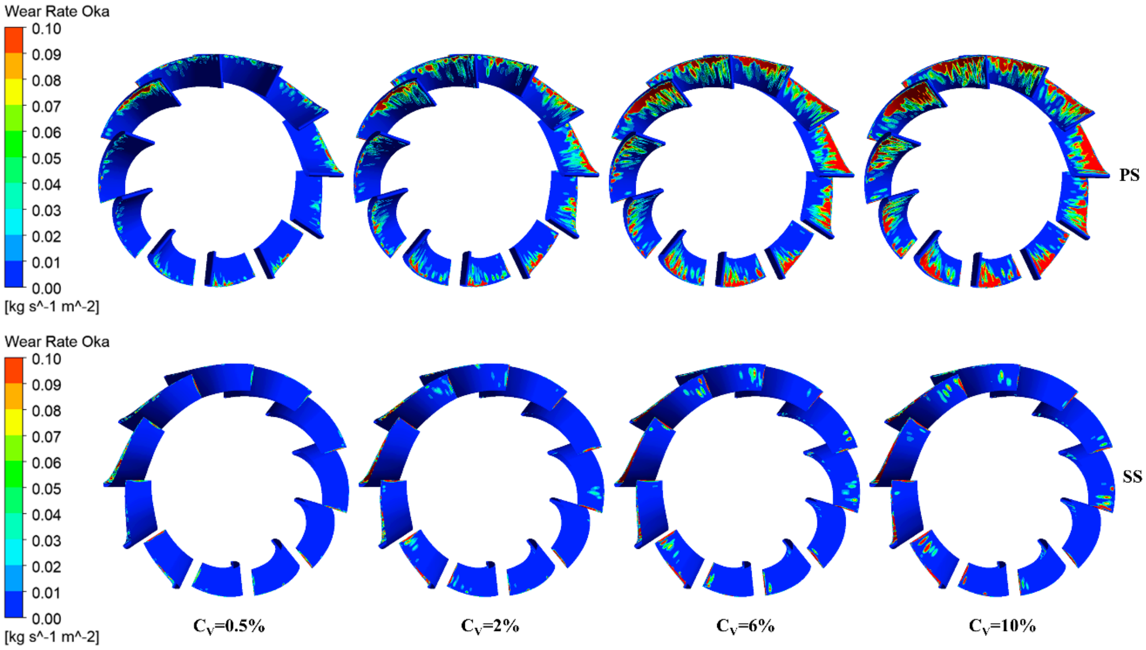

Figure 20. Wear distribution of diffuser blade surface.

6.2. Analysis of Blade Surface Wear Factors

The diameter, concentration, and Reynolds number of the sand particles were carefully selected to conduct a comprehensive analysis of the predominant factors influencing blade surface wear. Figure 21 shows the wear rate and the distribution of the three variables on the pressure surface of the impeller blade. According to the wear distribution of the impeller pressure surface, the pressure surface is divided into two parts: V_1 and V_2, respectively, as marked in Figure 21. The wear in the V_1 area is more severe than that in the V_2 area, as depicted in Figure 21. The sand particles impacting V_1 exhibit smaller diameters compared to those impacting V_2, while the sand concentration in V_1 is comparatively lower than that in V_2. However, the sand grains in the V_1 area exhibit a higher Reynolds number, indicating that they experience greater fluid-induced drag force and possess larger momentum upon impact with the surface. The Reynolds number of sand emerges as the predominant factor influencing wear on the pressure surface of impeller blades, thus summarizing the key aspect under consideration.

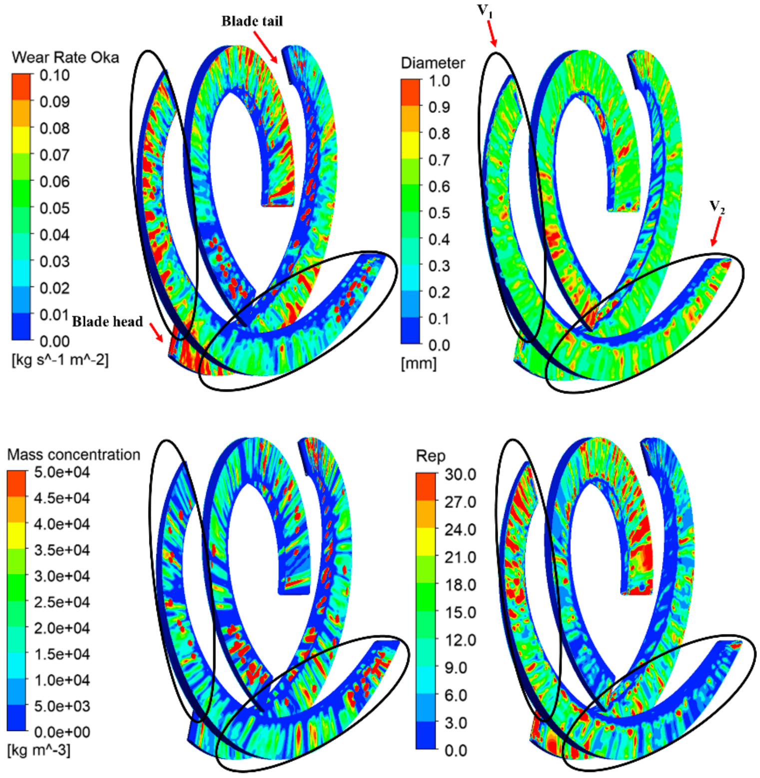

Figure 21. The wear rate, sand particle diameter, sand particle concentration, and sand particle Reynolds number as distributed on the impeller pressure surface.

The distribution of wear rate, sand particle diameter, sand particle concentration, and sand particle Reynolds number on the suction surface of the impeller blade is illustrated in Figure 22. On the suction surface of the blade, both the sand particle diameter and sand particle Reynolds number in the V_1 area are smaller compared to those in the V_2 area; however, the sand particle concentration on the surface is significantly higher than that in the V_2 area. This suggests that wear on the suction surface is more influenced by sand particle concentration rather than sand particle diameter and the Reynolds number. Additionally, as depicted in Figure 10, the presence of sand clusters near the blade suction surface results in localized areas of point-like wear.

The analysis of wear on the diffuser surface was also conducted, as depicted in Figure 23. The areas where wear occurs on the diffuser pressure surface do not completely coincide with the areas characterized by larger sand particle diameters and Reynolds numbers. However, the wear spots on the blade surface correspond to locations of high sand particle concentration, suggesting that the wear of the diffuser pressure surface is predominantly influenced by sand particle concentration.

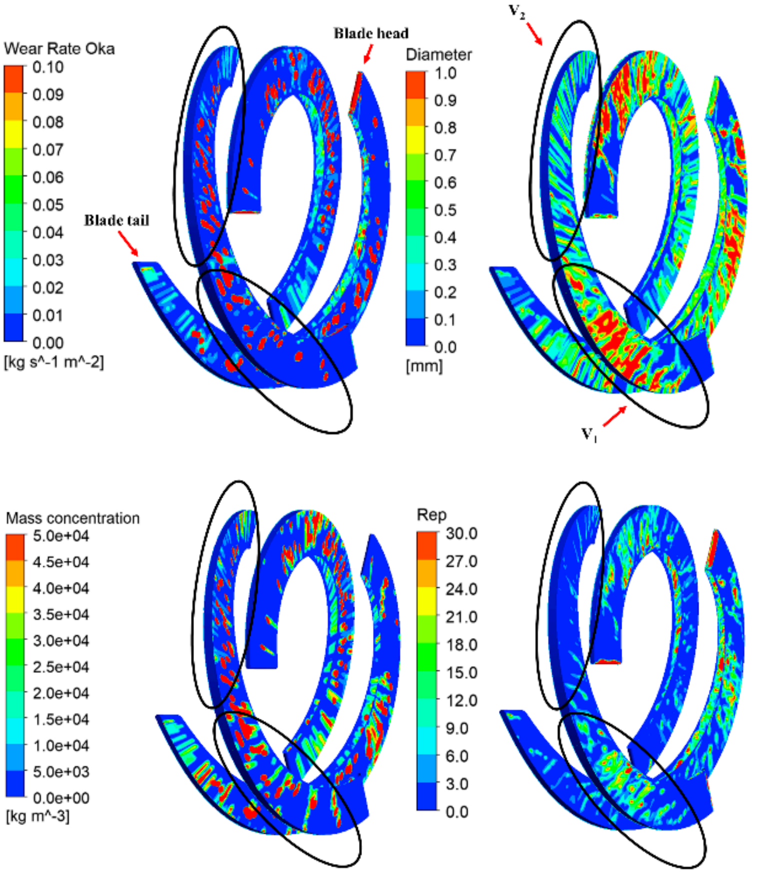

Figure 22. The wear rate, sand particle diameter, sand particle concentration, and sand particle Reynolds number as distributed on the impeller suction surface.

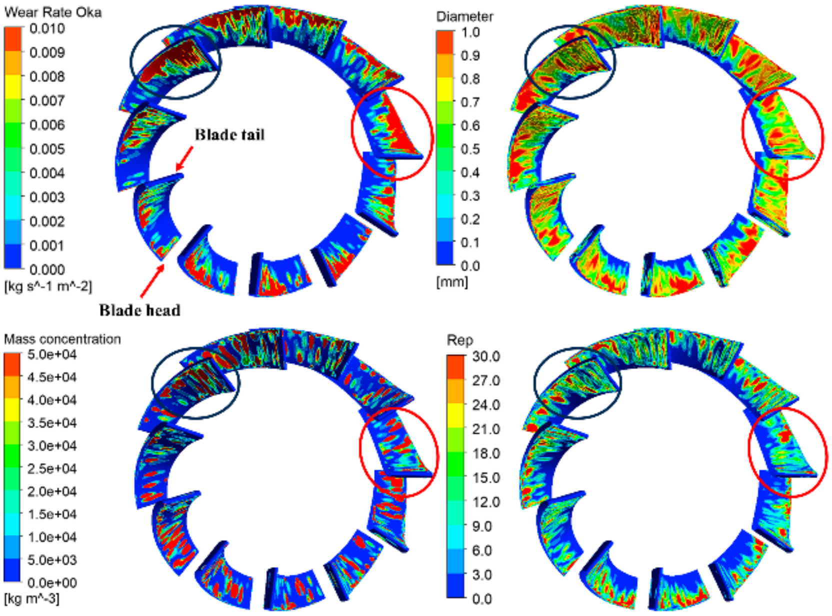

Figure 23. The wear rate, sand particle diameter, sand particle concentration, and sand particle Reynolds number as distributed on the diffuser pressure surface.

The distribution of wear rate, sand particle diameter, sand particle concentration, and sand particle Reynolds number on the suction surface of the diffuser is illustrated in Figure 24. The analysis of Figure 24 reveals a low degree of overlap between the region with the larger sand particle diameter and the area exhibiting surface wear. Moreover, the distribution patterns of sand particle concentration and the sand particle Reynolds number align more closely with the wear area, particularly in terms of sand particle concentration. The wear of the suction surface is primarily influenced by the concentration of sand particles, with the Reynolds number of the sand particles being a secondary factor. The local enlarged picture of the blade head reveals that the severe wear is primarily attributed to the high Reynolds number of sand particles, resulting in pronounced surface degradation due to their high impact velocity.

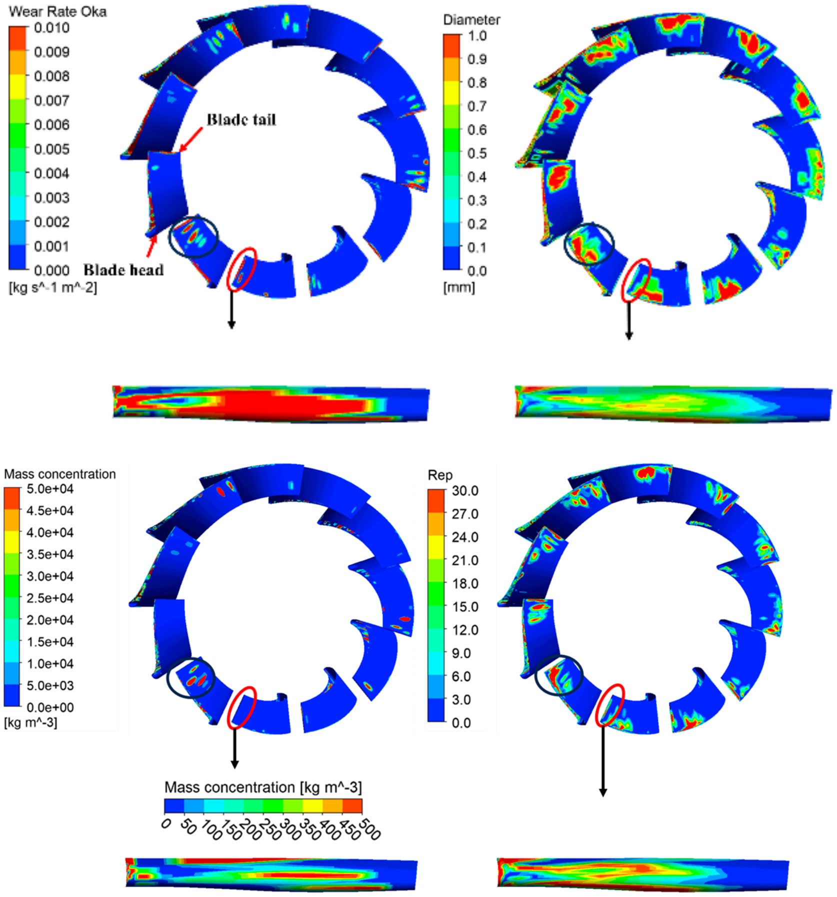

Figure 24. The wear rate, sand particle diameter, sand particle concentration, and sand particle Reynolds number as distributed on the diffuser suction surface.

In order to gain a deeper understanding of the relationship between blade surface wear and sand particle diameter, sand particle concentration, and sand particle Reynolds number, the impeller blade and diffuser blade were divided into ten isometric zones (Q_1~Q_{20}) along the axial direction of the multiphase pump, as illustrated in Figure 25. The average wear rate, sand particle diameter, sand particle concentration, and sand particle Reynolds number were individually recorded for each of these twenty zones.

The average wear rate, sand particle diameter, sand particle concentration, and sand particle Reynolds number in each subarea are depicted in Figure 26. Additionally, the change curve of blade surface area is presented to elucidate the intrinsic relationship between the wear rate on the blade surface and factors such as sand particle diameter, sand particle concentration, and sand particle Reynolds number. As can be seen from Figure 26, from the head of the impeller blade to the tail of the diffuser, the wear rate shows a trend of rapid decrease followed by a slow decrease. The wear rate trend can be elucidated by the combined influence of sand particle diameter, sand particle concentration, and sand particle Reynolds number. The Reynolds number of the sand particles exhibits a continuous decrease from Q_1 to Q_{10}, while the concentration and diameter of sand particles remain essentially unchanged. However, it is noteworthy that the wear rate demonstrates a consistent decline throughout this range, suggesting a significant influence of the Reynolds number on wear rate between Q_1 and Q_{10}. The wear rate between Q_{11} and Q_{20} exhibits minimal variation, and its variation law is inconsistent with the variation of sand Reynolds number, sand diameter, and sand concentration, indicating that the wear rate in this area is affected by the joint effect of sand diameter, sand concentration, and the sand Reynolds number. The wear rate in the impeller is primarily influenced by the sand Reynolds number, while the diffuser domain is subject to a combined influence of sand diameter, sand concentration, and the sand Reynolds number.

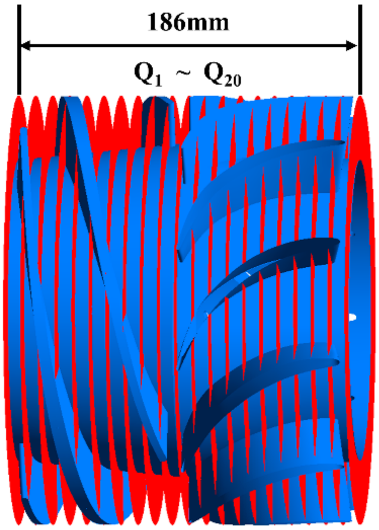

Figure 25. Schematic diagram of blade segmentation.

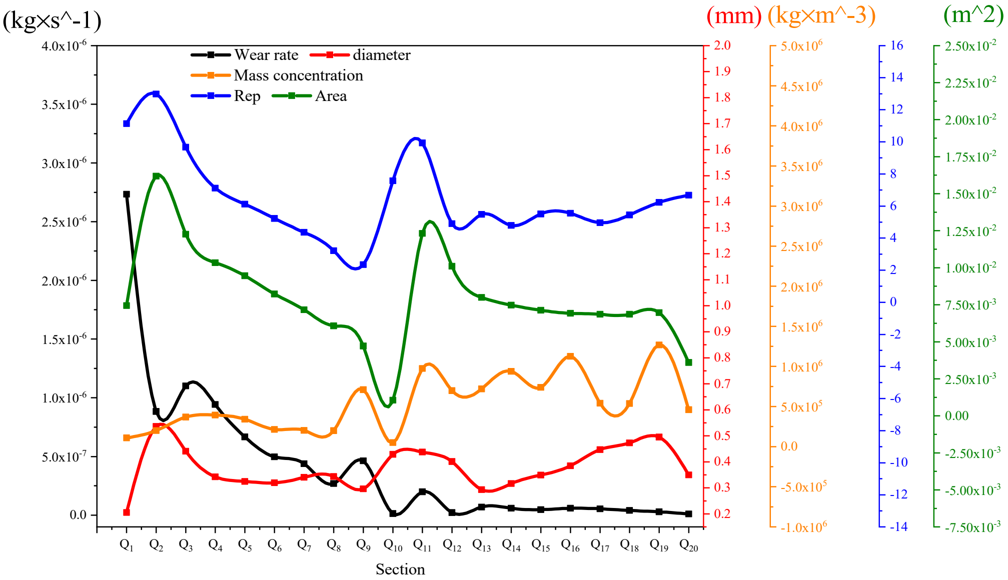

Figure 26. Change curve of wear rate per unit time, sand particle diameter, sand particle concentration, and sand particle Reynolds number.

7. Conclusions

(1) With the increase in sand concentration, the impeller blade's leading edge and the diffuser runner's central region exhibit primary areas of sand aggregation, consistently demonstrating a higher number of sand particles within the diffuser compared to those within the impeller at all concentrations. The distribution of sand particles exhibits a relatively dispersed pattern at the inlet of the impeller domain, while gradually adhering to the hub in pieces during their movement from the inlet to the outlet. Moreover, there is a

gradual decrease in the concentration of sand particle accumulation from the hub towards the shroud. In the diffuser domain, the distribution of sand particles is predominantly concentrated in the central area of the flow passage and along the shroud. Moreover, it is evident that the velocity of sand particles in this region is significantly lower compared to that observed in the impeller domain. Additionally, within the flow passage itself, a noticeable decrease in sand particle velocity can be observed when compared to that at the shroud.

(2) The distribution of shear flow in the impeller domain is highly consistent with that of the sand particles. In the diffuser domain, the large vortex causes the formation of sand lumps in the middle of the flow passage, that is, the middle of the vortex. The movement trajectory of sand particles is found to be correlated with the shear flow, while the vortex motion within the impeller domain results in a more concentrated distribution of sand particles. In the diffuser domain, both sand distribution and vortex distribution exhibit disorderly patterns from inlet to outlet. While the sand distribution at the inlet maintains its characteristics from the impeller domain, in the diffuser domain, sand is mainly distributed in the middle of the vortex within the flow channel, whereas at the outlet, it is distributed along walls. The influence of the vortex in the diffuser domain on the movement of sand particles is evident as these particles are observed to be entrained by the vortex. The main reason is that the shear vortex energy in the impeller is larger and the rotating vortex energy in the diffuser is larger, so the movement of sand particles in different flow channels is affected by different vortices.

(3) When the sand concentration is low, the wear area of the impeller blade's pressure surface is smaller than that of its suction surface, with predominant wear at the tail of the blade for the pressure surface and more concentrated in the middle for the suction surface. As sand concentration increases, noticeable wear appears on the front edge of the pressure surface. On the suction surface, there is minimal change in wear area with increasing concentration but a significant increase in wear degree. The diffuser's pressure surface experiences noticeably greater wear compared to its suction surface, primarily distributed at its shroud. With increasing sand concentration, this wear area gradually expands towards the middle of the blade. Wear on the diffuser's suction surface occurs on its inlet side and shows minimal increase in size as sand concentration rises. The impeller domain exhibits more severe wear both in terms of area and degree compared to that observed in the diffuser domain.

(4) In the impeller, the wear of the first half of the blade is more severe than that of the second half. The sand Reynolds number is identified as the primary factor influencing wear on the pressure surface of impeller blades. On the suction surface of impeller blades, wear is predominantly influenced by sand concentration rather than sand diameter and the Reynolds number, with clumping near this surface resulting in localized areas of increased wear. Within the diffuser domain, wear on the pressure surface is significantly affected by sand concentration. On its suction surface, wear is primarily impacted by sand concentration, followed by the Reynolds number. The substantial wear observed at the heads of the diffuser blades can be attributed to the high sand Reynolds numbers causing significant impact velocities and, subsequently, severe abrasion. Wear rates exhibit a rapid decrease from the impeller blade head to the diffuser tail, followed by a slower decline. While in the impeller domain, the wear rate mainly depends on the sand Reynolds number, in contrast, within the diffuser domain, it results from the combined effects of sand diameter, sand concentration, and the sand Reynolds number.

Author Contributions: Conceptualization, G.S.; Methodology, X.G. and G.S.; Software, X.G. and X.Y.; Validation, X.G.; Formal analysis, Y.X.; Resources, Y.X.; Data curation, Y.X. and X.Y.; Writing—original draft, X.G.; Writing—review & editing, G.S.; Visualization, X.Y. All authors have read and agreed to the published version of the manuscript.

Funding: This work was supported by the Sichuan Natural Science Foundation Outstanding Youth Science Foundation (2024NSFJQ0012) and the Key project of Regional Innovation and Development Joint Fund of National Natural Science Foundation (U23A20669).

Informed Consent Statement: Not applicable.

Data Availability Statement: Datasets generated during the current study are available from the corresponding author on reasonable request.

Conflicts of Interest: The authors declare that they have no known competing financial interests or personal relationships that could have appeared to influence the work reported in this paper. Written informed consent for publication of this paper was obtained from the Xihua University and all authors.

References

1. Othayq, M.M.; Bilal, F.S.; Sedrez, T.A.; Shirazi, S.A. Experimental and Numerical Assessments on Solid Particle Erosion in Upward Vertical-Horizontal and Horizontal-Vertical Downward Elbows for Multiphase and Gas-Sand Flows. *Wear* **2023**, *524*, 204812. [CrossRef]
2. Rajkumar, Y.; Shirazi, S.A.; Karimi, S. Effect of Pipe Size on Erosion Measurements and Predictions in Liquid-Dominated Multiphase Flows for the Elbows. *Wear* **2023**, *523*, 204797. [CrossRef]
3. Espinoza-Jara, A.; Walczak, M.; Brevis, W.; Messa, G.V. Erosion by Turbulence: Discovering the Counter-Wise Vortex Events and Their Effect on Wear. *Wear* **2023**, *530–531*, 204988. [CrossRef]
4. Shi, B.; Xue, K.; Pan, J.; Zhang, X.; Ying, R.; Wu, L.; Zhang, Y. Liquid/Solid Flow Field in a Centrifugal Pump with Different Impeller Blade Types by PIV. *Meas. Control* **2021**, *54*, 1219–1233. [CrossRef]
5. Kang, C.; Li, Q.; Li, M.; Teng, S. Deposition of Solid Particles Exposed to the Suction of Dual Pumps in the Tank of a Pumping Station. *Powder Technol.* **2020**, *361*, 727–738. [CrossRef]
6. Wang, K.; Hu, J.; Liu, H.; Zhang, Z.; Zou, L.; Lu, Z. Research on the Deposition Characteristics of Integrated Prefabricated Pumping Station. *Symmetry* **2020**, *12*, 760. [CrossRef]
7. Chen, Y.; Xiong, H.; Cheng, H.; Yu, C.; Xie, J. Effect of Particle Motion on the Hydraulic Collection of Coarse Spherical Particles. *Acta Mech. Sin.* **2020**, *36*, 72–81. [CrossRef]
8. Wang, P.; Zhu, X.; Li, Y. Analysis of Flow and Wear Characteristics of Solid-Liquid Two-Phase Flow in Rotating Flow Channel. *Processes* **2020**, *8*, 1512. [CrossRef]
9. Hu, Q.; Chen, J.; Deng, L.; Kang, Y.; Liu, S. CFD-DEM Simulation of Backflow Blockage of Deep-Sea Multistage Pump. *J. Mar. Sci. Eng.* **2021**, *9*, 987. [CrossRef]
10. Calderon-Hernandez, J.W.; Sinatora, A.; de Melo, H.G.; Chaves, A.P.; Mano, E.S.; Leal Filho, L.S.; Paiva, J.L.; Braga, A.S.; Souza Pinto, T.C. Hydraulic Convey of Iron Ore Slurry: Pipeline Wear and Ore Particle Degradation in Function of Pumping Time. *Wear* **2020**, *450*, 203272. [CrossRef]
11. Shen, Z.; Chu, W.; Li, X.; Dong, W. Sediment Erosion in the Impeller of a Double-Suction Centrifugal Pump—A Case Study of the Jingtai Yellow River Irrigation Project, China. *Wear* **2019**, *422*, 269–279. [CrossRef]
12. Peng, G.; Huang, X.; Zhou, L.; Zhou, G.; Zhou, H. Solid-Liquid Two-Phase Flow and Wear Analysis in a Large-Scale Centrifugal Slurry Pump. *Eng. Fail. Anal.* **2020**, *114*, 104602. [CrossRef]
13. Perea Serrano, R.O.; Santos, L.P.; de Faria Viana, E.M.; Pinto, M.A.; Martinez, C.B. Case Study: Effects of Sediment Concentration on the Wear of Fluvial Water Pump Impellers on Brazil's Acre River. *Wear* **2018**, *408*, 131–137. [CrossRef]
14. Walker, C.I.; Robbie, P. Comparison of Some Laboratory Wear Tests and Field Wear in Slurry Pumps. *Wear* **2013**, *302*, 1026–1034. [CrossRef]
15. Li, Y.; Zeng, X.; Lv, W.; He, Z. Centrifugal Pump Wear for Solid-Liquid Two-Phase Flows Based on Computational Fluid Dynamics-Discrete Element Method Coupling. *Adv. Mech. Eng.* **2020**, *12*, 1687814020937951. [CrossRef]
16. Fujisawa, K. On Erosion Transition from the Incubation Stage to the Accumulation Stage in Liquid Impingement Erosion. *Wear* **2023**, *528*, 204952. [CrossRef]
17. Wang, B.; Guo, Y.; Zhang, Z.; Yi, X.; Wang, D. Investigation of Cryogenic Friction and Wear Properties of Invar 36 Alloy against Si3N4 Ceramic Balls. *Wear* **2023**, *518*, 204648. [CrossRef]
18. Bueno, A.H.S.; Solis, J.; Zhao, H.; Wang, C.; Simoes, T.A.; Bryant, M.; Neville, A. Tribocorrosion Evaluation of Hydrogenated and Silicon DLC Coatings on Carbon Steel for Use in Valves, Pistons and Pumps in Oil and Gas Industry. *Wear* **2018**, *394*, 60–70. [CrossRef]
19. Luo, K.; Wang, Y.; Liu, H.; Dular, M.; Chen, J.; Zhang, Z. Effect of Coating Thickness on a Solid-Liquid Two-Phase Flow Centrifugal Pump under Water Medium. *Stroj. Vestn. J. Mech. Eng.* **2019**, *65*, 251–261. [CrossRef]
20. Wang, L.; Li, B.; Zhao, W. Dynamics and Wear Analysis of Hydraulic Turbines in Solid-Liquid Two-Phase Flow. *Open Phys.* **2019**, *17*, 790–796. [CrossRef]
21. Tarodiya, R.; Gandhi, B.K. Numerical Simulation of a Centrifugal Slurry Pump Handling Solid-Liquid Mixture: Effect of Solids on Flow Field and Performance. *Adv. Powder Technol.* **2019**, *30*, 2225–2239. [CrossRef]

22. Wang, K.; Bao, H.; Liu, H.; Zhang, Z.; Hu, J. Influence of the Installation Position of Submersible Pumps on Deposition Characteristics in Prefabricated Pumping Stations. *Symmetry* **2020**, *12*, 1347. [CrossRef]
23. Wang, Y.; Tao, R.; Han, C.; Li, W.; He, T.; Zhu, Z. Numerical Study on Flow and Wear Characteristics of Dense Fine Particle Solid-Liquid Two-Phase Flow in Centrifugal Pump. *AIP Adv.* **2022**, *12*, 045109. [CrossRef]
24. Li, Y.; Liu, S.; Hu, X. Research on Rotating Speed's Influence on Performance of Deep-Sea Lifting Motor Pump Based on DEM-CFD. *Mar. Georesources Geotechnol.* **2019**, *37*, 979–988. [CrossRef]
25. Huang, S.; Huang, J.; Guo, J.; Mo, Y. Study on Wear Properties of the Flow Parts in a Centrifugal Pump Based on EDEM-Fluent Coupling. *Processes* **2019**, *7*, 431. [CrossRef]
26. Noon, A.A.; Kim, M.-H. Erosion Wear on Centrifugal Pump Casing Due to Slurry Flow. *Wear* **2016**, *364*, 103–111. [CrossRef]
27. Chen, W.; Xu, H.-L.; Yang, F.; Rao, X.; Zhou, Y.-X.; Hu, D.; Lin, P. Research on the Transportation and Flow Characteristics of Deep-Sea Ore Transportation Equipment. *Appl. Ocean Res.* **2021**, *113*, 102765. [CrossRef]
28. Wang, Y.; Wang, X.; Chen, J.; Li, G.; Liu, H.; Xiong, W. An Experimental Insight into Dynamic Characteristics and Wear of Centrifugal Pump Handling Multi-Size Particulate Slurry. *Eng. Fail. Anal.* **2022**, *138*, 106303. [CrossRef]
29. Tang, C.; Kim, Y.-J. CFD-DEM Simulation for the Distribution and Motion Feature of Solid Particles in Single-Channel Pump. *Energies* **2020**, *13*, 4988. [CrossRef]
30. Gu, Y.; Liu, N.; Mou, J.; Zhou, P.; Qian, H.; Dai, D. Study on Solid-Liquid Two-Phase Flow Characteristics of Centrifugal Pump Impeller with Non-Smooth Surface. *Adv. Mech. Eng.* **2019**, *11*, 1687814019848269. [CrossRef]
31. Gu, Y.; Yan, M.; Yu, J.; Xia, K.; Ma, L.; Mou, J.; Wu, D.; Tang, J. Effect of the Bionic Circular Groove Non-Smooth Structure on the Anti-Wear Performance of the Two-Vane Pump. *Lubricants* **2022**, *10*, 231. [CrossRef]
32. Xu, H.-L.; Chen, W.; Xu, C. Cavitation Performance of Multistage Slurry Pump in Deep-Sea Mining. *AIP Adv.* **2019**, *9*, 105024. [CrossRef]
33. Zhang, C.; Xu, S.; Yu, P. Numerical Analysis of the Effects of Gas-Phase Properties on the Internal Characteristics and Wear in a Centrifugal Pump. *Aquac. Eng.* **2020**, *91*, 102126. [CrossRef]
34. Tao, Y.; Bai, Y.; Wu, Y. Influence of Blade Thickness on Solid-Liquid Two-Phase Flow and Impeller Wear in a Ceramic Centrifugal Slurry Pump. *Processes* **2021**, *9*, 1259. [CrossRef]
35. Peng, G.; Chen, Q.; Bai, L.; Hu, Z.; Zhou, L.; Huang, X. Wear Mechanism Investigation in a Centrifugal Slurry Pump Impeller by Numerical Simulation and Experiments. *Eng. Fail. Anal.* **2021**, *128*, 105637. [CrossRef]
36. Romo, S.A.; Santa, J.F.; Giraldo, J.E.; Toro, A. Cavitation and High-Velocity Slurry Erosion Resistance of Welded Stellite 6 Alloy. *Tribol. Int.* **2012**, *47*, 16–24. [CrossRef]